

Enhanced signal coupling in wide-field fiber-coupled imagers

Ashkan Arianpour,* Nojan Motamedi, Ilya P. Agurok, and Joseph E. Ford

Electrical and Computer Engineering Department, University of California San Diego, 9500 Gilman Drive, La Jolla, California 92093, USA

*aarianpo@ucsd.edu

Abstract: Some high-performance imaging systems, including wide angle “monocentric” lenses made of concentric spherical shells, form a deeply curved image surface coupled to focal plane sensors by optical fiber bundles with a curved input and flat output face. However, refraction at the angled input facet limits the range of input angles, even for fiber bundles with numerical aperture 1. Here we investigate using a curved beam deflector near the focal surface to increase the field of view and improve spatial resolution at the edges of the field of view. We show the field of view of such an imager can be increased from approximately 60° (full width at half maximum intensity) to over 90° using an embossed refractive microprism array, where the prism angle varies across the aperture to maintain coupling. We describe a proof-of-principle experiment using a $f = 17.8\text{mm}$ fiber-coupled monocentric singlet lens, and show that a local region of microprisms embossed into a thin layer of SU-8 photopolymer can increase the field of view by 50%.

©2015 Optical Society of America

OCIS codes: (080.3620) Lens system design; (110.2350) Fiber optics imaging; (220.4830) Systems design.

References and links

1. W. Y. Lau, C. K. Leow, and A. K. C. Li, “History of endoscope and laparoscopic Surgery,” *World of Surgery* **21**(4 Issue 4), 444–453 (1997).
2. J. A. Waidelich, Jr., “Spherical lens imaging device,” U.S. patent 3,166,623 (19 January 1965).
3. R. Kingslake, *A History of the Photographic Lens* (Academic, 1989), pp. 49–67.
4. T. S. Axelrod, N. J. Colella, and A. G. Ledebuhr, “The wide-field-of-view camera,” in *Energy and Technology Review* (Lawrence Livermore National Laboratory, 1988).
5. J. F. Kordas, I. T. Lewis, B. A. Wilson, D. P. Nielsen, H. S. Park, R. E. Priest, R. Hills, M. J. Shannon, A. G. Ledebuhr, and L. D. Pleasance, “Star tracker stellar compass for the Clementine mission,” *Proc. SPIE* **2466**, 70–83 (1995).
6. J. Ford, I. Stamenov, S. Olivas, G. Schuster, N. Motamedi, I. Agurok, R. Stack, A. Johnson, and R. Morrison, “Fiber-coupled Monocentric Lens Imaging,” in *Imaging and Applied Optics*, OSA Technical Digest (2013).
7. I. Stamenov, A. Arianpour, S. J. Olivas, I. P. Agurok, A. R. Johnson, R. A. Stack, R. L. Morrison, and J. E. Ford, “Panoramic monocentric imaging using fiber-coupled focal planes,” *Opt. Express* **22**(26), 31708–31721 (2014).
8. J. E. Shields, M. E. Karr, R. W. Johnson, and A. R. Burden, “Day/night whole sky imagers for 24-h cloud and sky assessment: history and overview,” *Appl. Opt.* **52**(8), 1605–1616 (2013).
9. J. J. Hancock, *The Design, Fabrication, and Calibration of a Fiber Filter Spectrometer*. Doctoral dissertation. University of Arizona, Tucson, 2012.
10. A. Cozannet and M. Treheux, “Skew rays in optical fibers,” *Appl. Opt.* **14**(6), 1345–1350 (1975).
11. L. Jing, H. Liu, H. Zhao, Z. Lu, H. Wu, H. Wang, and J. Xu, “Design of novel compound Fresnel lens for high-performance photovoltaic concentrator,” *Int. J. Photoenergy* **2012**, 1 (2012).
12. C. Reardon, A. Di Falco, K. Welna, and T. Krauss, “Integrated polymer microprisms for free space optical beam deflecting,” *Opt. Express* **17**(5), 3424–3428 (2009).
13. A. Smolyaninov, L. Pang, L. Freeman, M. Abashin, and Y. Fainman, “Broadband metacoaxial nanoantenna for metasurface and sensing applications,” *Opt. Express* **22**(19), 22786–22793 (2014).

1. Introduction

Fiber-bundle imaging has a long history, including medical applications like endoscopy and laparoscopy, where fiber bundles transport a remote image plane for detection or viewing [1]. Imaging fiber bundles can also couple light between non-planar image surfaces, including the spherically curved image formed by “monocentric” hemispherical objective lenses [2,3]. Conventional wide-angle lenses, especially extreme “fisheye” lenses, increase field of view at a cost in light collection relative to their large input aperture and volume, producing distorted and relatively low-resolution planar images. Using spherical optical surfaces eliminates the most problematic geometrical aberrations and potentially allows high-resolution wide angle imaging. Deeply curved image sensors cannot be fabricated using conventional semiconductor wafer processing, but a fiber bundle can connect a planar sensor to the spherical image surface. Such an imager was first made by Lawrence Livermore Labs [4]. Light incident on a curved input surface of numerical aperture 1 fiber was coupled into a dense array of straight N.A. 1 fibers, and then transmitted to a flat output surface connected to a 576x384 pixel CCD focal plane. However, the Clementine “Star Tracker” [5] had only a 52° field of view, which took little advantage of the potential of the monocentric lens configuration. The field of view limitation of the single-sensor Clementine star tracker came from refraction at the input face of the curved fiber bundle. For a flat NA = 1 fiber, light couples for angles ranging from 0° to 90°. In a curved-face fiber bundle, light in general is incident on an angled facet. Figure 1 shows that at some angles the refracted light can exceed the internal critical angle resulting in high loss, and the transmitted signal may reflect from the output face of the fiber, or emit into such a large angle to interfere with focal plane sensing. A finite thickness between the bundle and the sensor prevents the fiber bundle from making direct contact with the active region of a sensor. Given this physical gap, the divergence of light can potentially overlap multiple pixels in the sensor, effectively blurring the impulse response and reducing resolution.

We modeled a F/2 nearly diffraction-limited monocentric lens system and fiber array (NA = 1, $n_{\text{core}} = 1.81$, $n_{\text{cladding}} = 1.48$) using Photon Engineering’s FRED non-sequential ray trace software, calculating the coupling efficiency through a 3x3 fiber array positioned at different field angles. The coupling efficiency as a function of field angle for the system seen in Fig. 2. A significant drop in intensity is observed as the fields approach the complement to the critical angle of the system (35° with respect to the fiber’s axis) and a negligible amount of power couples into the fibers beyond that point. Both coupling efficiency and divergence between the fiber bundle and focal plane sensor means that a wide emission angle causes a

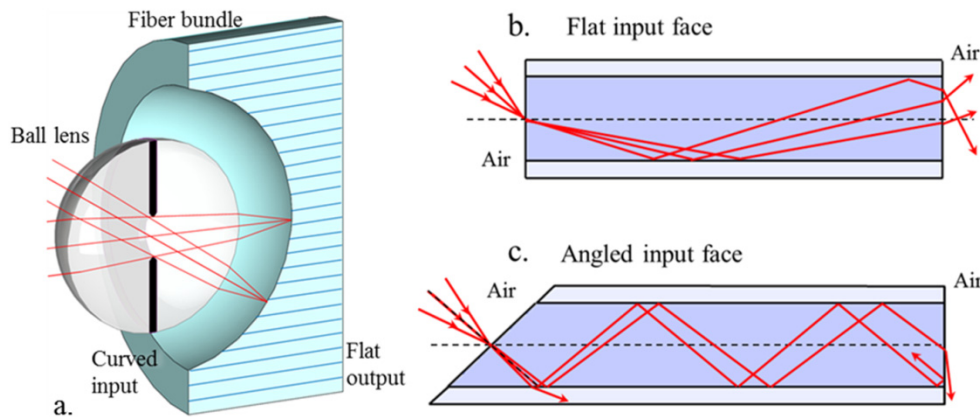


Fig. 1. a) 3-D geometrical schematic of monocentric fiber coupled imager, b) shows how an off-axis focusing beam would couple into a fiber bundle with a planar face, while c) shows how the locally angled input face of the curved-face fiber bundle interferes with signal coupling, and limits the maximum angle achievable with a simple straight fiber bundle.

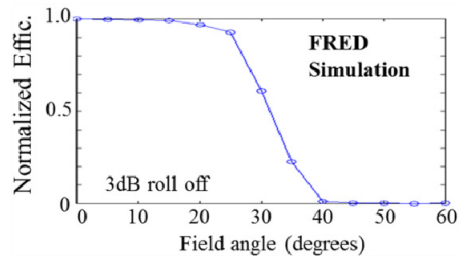


Fig. 2. FRED simulation of coupling efficiency of an F/2 nearly diffraction limited monocentric lens with 2.5 μ m pitch fibers. The power drops off dramatically as the field approaches the 35 $^\circ$, the complement to the critical angle of the fiber bundle.

broadening in the point spread function. Therefore, these fiber coupling effects must be addressed to make effective use of the principle performance advantage of the monocentric objective lens, so that it can maintain high-resolution over a wide field of view.

Recently, we demonstrated a compact 30 Megapixel monocentric imager with a 120 $^\circ$ field of view using multiple fiber-coupled CMOS image sensors [6,7]. The imager divides a single image surface into 6 sections, with curved face fiber bundles closely tiled across the curved image surface. The sensors are arranged such that each section covered less than 30 $^\circ$ diagonal angle, and so they maintain good illumination uniformity. One difficulty with this approach is the fabrication and mechanical alignment between the bundles; even a small gap causes loss of image data. Another alternative is to use a fully 3-dimensional waveguide array. If the fibers are internally curved so that the input fiber axis is close to normal to the focused light beam, and the output fiber axis is close to normal to the focal plane sensor, then the incident light is efficiently coupled and the propagating light mode adiabatically transformed to a desirable emission and efficiency coupling to the focal plane sensor [6,7]. This solution can potentially enhance the coupling efficiency for a wide range of angles, but the fabrication of the required 3-D waveguide structure is more challenging than of the straight fiber bundles. Recently, research groups have used tapered fiber bundles with flat input and output surfaces for relay imaging and demagnifying the size of the image, but do not use a curved input surface or monocentric lens for reducing the optical components [8].

A different approach to enable coupling of a wide range of incident angle light into a straight fiber bundle is to modify the beam incidence angle just before it is incident on the fiber face. The challenge is to create a structure near the interface of the input fiber that can either refract or diffract the focusing beam at angles to increase the coupling efficiency and reduce the divergence angle for a single curved-face fiber bundle. As Fig. 3(c) shows, this structure can be located at or before the spherical image surface. A deflector located at the image surface may or may not maintain spatial wavefront coherence. For example, a diffuse scattering surface such as a roughened fiber input face will send at least some of the incident light into guided modes. We experimentally tested this approach, but found it provided only a slight enhancement in wide-angle signal coupling, and a negligible reduction in the divergence of the exiting beam. As an alternative, a radial beam deflector at or near the image plane that maintains spatial coherence of the focusing wavefront can increase coupling efficiency and also can be adjusted to reduce the divergence at the output of the fiber. Such a beam deflector can be refractive or diffractive. A refractive surface (e.g., microprism) offers a broad spectral response, and may potentially be manufactured at low cost by embossing or molded onto the curved surface. This method is preferable over the sectioned or 3-D waveguide structure since it uses current manufacturing processes, and can potentially be accomplished at the wafer-level. In this paper, we investigate this approach, and show that a refractive micro-prism array surface can redirect the incoming focusing beam at the extreme angles to improve system coupling efficiency and increase the maximum field of view from

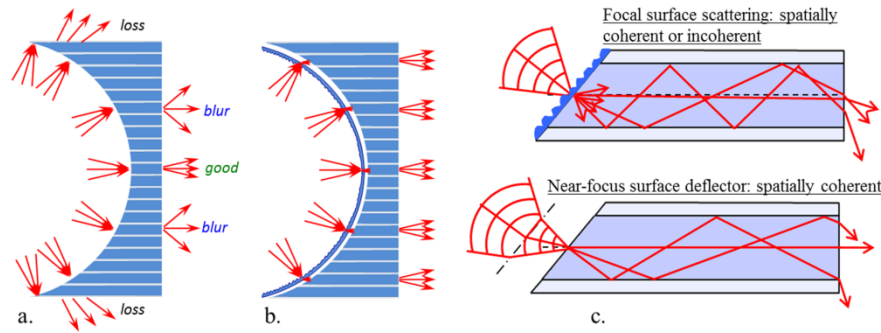


Fig. 3. Illustration of light coupling into fibers at various angles for a) bare curved-face fiber bundle, b) surface-enhanced curved-face fiber bundle, and c) enlarged view of a scattering facet surface and a beam deflective structure modifying the focusing beam to enhance coupling in an angled facet.

approximately 50° to 90° . In Section 2, we compare the response of both flat and curved-face fiber bundles with $NA = 1$ fibers using both a non-sequential simulation and experimental characterization. In Section 3, we present an analytical solution to design of the blaze angle of the micro-prism array, with an analysis of the effect on system performance. In Section 4, we demonstrate a proof of concept using a monocentric fiber-coupled imager with and without a region of embossed micro-prism array, then conclude in Section 5.

2. Modeling and characterization of fiber bundles

Examining the difference in divergence angle for the two geometries (flat and curved-face) reveals the system's response in monocentric fiber coupled imaging, and provides metrics for engineering the radial micro-prism array on a curved-face bundle. To begin, we investigated the coupling and emission response of flat and curved-face fiber bundles to an incident collimated beam. In a monocentric imaging system, a cone of light is incident on a curved image plane with the chief ray normal to the imaging surface for all field angles. Substituting a curved-face fiber bundle for an image surface, the chief rays are incident normal to the angled facets of the individual fibers. Evaluating the system with respect to the chief rays approximates the divergence and coupling efficiency for a given $F/\#$ imaging system using a curved-face fiber bundle.

Approximating the system using geometrical optics, Fig. 4 shows a FRED non-sequential ray-tracing simulation to view the cross section of the imager, and illustrate the divergence when exiting the fiber. The source was a monochromatic (532nm) collimated beam for field angles ranging from 0° to 45° . Each field angle was associated with a 3×3 array of cylindrical fibers for both the flat and curved-face geometries. The fiber's core and cladding ratio give a numerical aperture of one, and a pitch of $8\mu\text{m}$. For our calculations, we assumed the refractive indices of the fiber core and cladding are 1.81 and 1.48, based on published values for Schott's NA 1 fiber [9]. With these indexes, the critical angle is 54.85° with respect to the fiber side wall surface, or 35.15° with respect to the fiber's axis, which we call the axial critical angle. Placing the origin of the beam at the center of curvature of the curved face fiber bundle in Fig. 4(b) replicates the chief ray in a monocentric imaging system. The exiting beam in Fig. 4(a) is a hollow cone which subtends an angle equal to the incident angle of illumination for a flat fiber bundle. In a geometrical optical model, reflection from internal surfaces of the round fibers causes the propagating beam to retain angle relative to the fiber axis, but lose azimuthal orientation, such that the emitted beam is a hollow cone of light. A more accurate physical model, including diffraction, shows a similar effect even of square fibers, unless the fibers are very large compared to the illuminating wavelength.

For the flat-surfaced fiber bundle, shown in Fig. 4(a), rays incident normal to the angled facets refract at the air to fiber interface, and refract again when the light is emitted, returning

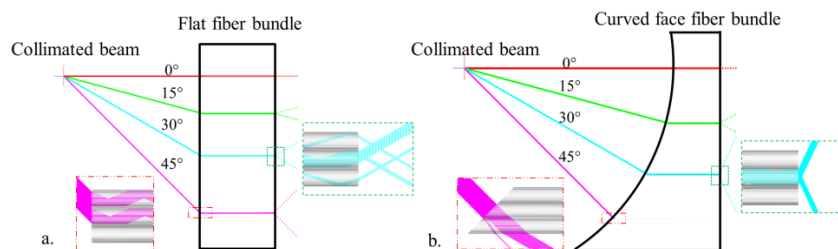


Fig. 4. FRED 2-dimensional simulation of laser (532nm) incident at 0°, 15°, 30°, 45° incident on a) flat bundle (NA = 1) and b) curved-face bundle (NA = 1) and exiting in air (n = 1).

to the original angle of incidence. For the fiber bundle with a curved input face, shown in Fig. 4(b), the divergence of emitted light increases with angle of incidence upon the curved bundle face. At 45°, the incident beam is not guided at all. If the illumination angle is larger than the axial critical angle (35° for the given core/cladding combination), total internal reflection no longer occurs, and the beam of light is refracted into the cladding and is no longer transmitted out of the corresponding core. A cross-sectional view as shown in Fig. 4 can be somewhat misleading. The physical structure in the fiber-coupled imager is three-dimensional, and the fibers are approximately cylindrical rods that will couple a portion of skew rays dependent on the angle entering the fiber, but the power coupled is significantly less than the rays close to the fiber axis [10].

We constructed an experimental test to match as closely as possible this simulation, using a plane-plane polished fiber bundle with 7-8 μm pitch fibers, and a spherically curved 17.8mm radius input face bundle with 7-8 μm pitch fibers, where both bundles were NA = 1. A 532nm laser with a Gaussian beam profile and spot size diameter of 1mm was incident on the input surfaces of the bundles at angles ranging from 0° to 45°. The experimental arrangement and measurement results are shown in Fig. 5. As the illumination angle nears the axial critical angle the coupled light approaches a divergence angle in air of 90°. To reduce the divergence angle, the output surface of the fiber bundle was bonded to a PMMA block (n = 1.49) with a diffusive rear surface. The intensity pattern on the rear surface was imaged with a limited numerical aperture DSLR camera with a CMOS sensor. Knowing the thickness of the PMMA block and the physical size of the image, we measured the relative intensity distribution across the scattering surface by integrating radially across the image and calculated the power distribution as a function of the angle for the beam as emitted directly from the fiber surface into air. Graphs in Fig. 5 depict the power distribution across the scene with relative peak intensities corresponding to the angle of divergence for all range of angles regarding both fiber bundles. Figure 5 shows that the flat fiber bundle couples light from 0° to 45° degrees with the peak energy distribution corresponding to the input angle of the respective beam. Most of the energy emitted from both bundles resided in the ring pattern, with negligible energy close to the center of the image except for near-normal incidence light. Light exiting the curved-face bundle diverged significantly as the angle of the input beam increases. The characteristic ring-pattern was not visible at 45°, and the signal power has dropped to near zero. The injection angle exceeded the axial critical angle of the fiber and significantly reduced the transmitted power at 45°. The number of fibers illuminated changes with the injection angle, but this has minimal impact on the emitted beam divergence.

Next, we considered the overall fiber-coupled imager structure, including the focus lens and sensor coupling. Figure 6 shows a three-dimensional system simulation in FRED, including a monocentric objective lens, fiber coupling, and high resolution image sensor. At each field angle, light is coupled in to the center of a 3x3 array of fibers with an 8 μm pitch, which couples out through a 10 μm gap with index 1.56 to an array of sensor pixels with 3.33 μm pitch. The imaging lens is a single glass BK7 sphere with a radius of 12.12mm and F/# 4.4,

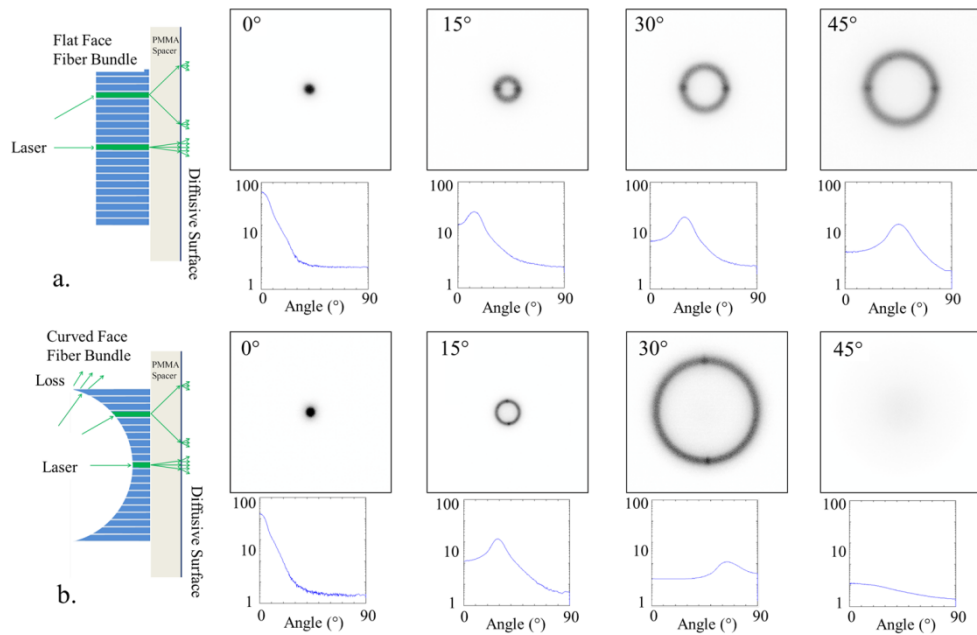


Fig. 5. Experimental demonstration of a 1mm spot size laser incident at angles of 0°, 15°, 30°, 45° on a) flat fiber bundle, b) curved-face fiber bundle. The contrast of these images have been inverted to show the regions of the dark rings where the intensity is greatest. The exit angles are measured by examining the peak relative intensities for their respective graphs below.

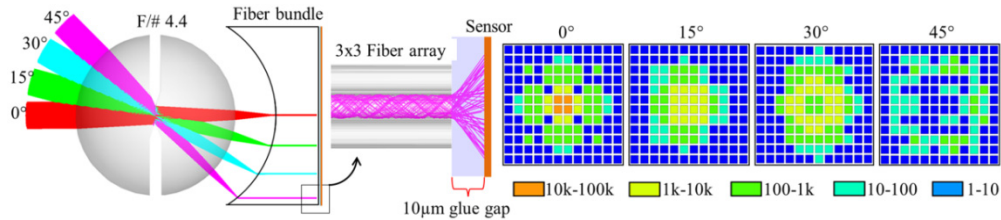


Fig. 6. FRED Simulation of fiber coupled monocentric imager's output response when coupled to a sensor with a 3.3µm pitch and 10µm glue thickness. The irradiance drops as a function of angle, and at 45° a negligible amount of energy is transmitted to the sensor.

and the incident light is a 532nm collimated source. As in our previous simulations, the fibers are NA = 1 with a core index of 1.81 and cladding of 1.48. Similar to the simpler collimated beam model results, as the field of view widens the size of the point spread function increases and the integrated intensity distribution across the detector decreases. The blurring due to the gap between the fiber bundle and sensor may be reduced; in fact the most recent experimental fiber-coupled image sensors had a physical adhesive layer which was approximately 5 µm thick [7]. But the loss in intensity when the field angles pass the axial critical angle is independent of the physical gap. A negligible amount of the incident energy is coupled at 45°, causing a nearly 100% vignetting in the monocentric fiber coupled imager. This is the motivation for using a beam deflector, such as a micro-prism array, to redirect incident light and increase coupled energy.

3. Radial micro-prism array design and analysis

We require an analytical approach for calculating the geometry of radial micro-prism array, especially the prism facet angle as a function of position across the curved input face. This is in general a function of the objective lens numerical aperture. However, the coupling for the

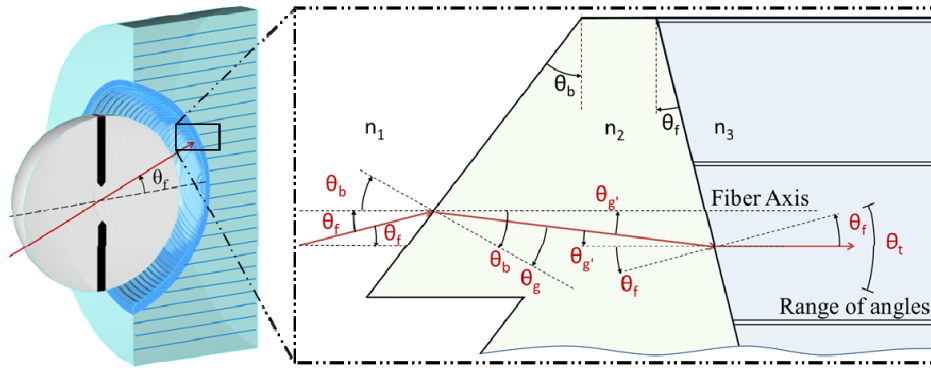


Fig. 7. Illustration of the cross-section of the radial microprism array and fiber bundle in conjunction with the monocentric lens, and a ray optics schematic of propagation of light through micro-prism array and fiber.

chief ray can be used as a straightforward design metric, accurate to within the cone-angle of the focusing light.

3.1 Analytical solution to micro-prism array

Figure 7 illustrates a system where chief rays passing through the monocentric system are incident on the radial micro-prism array and refracted into the fiber bundle. The facet angles of the individual fibers are approximately equal to the chief ray angle with respect to the object scene in an ideal monocentric system. This means that the chief ray is always incident normal to the fiber surface, transmitting through without refraction and incident on the core/cladding wall at same angle as the field. Adding a higher index micro-prism material onto the curved image surface refracts the rays at angles above the normal of the fiber facet. Rays that would have been above the axial critical angle can be totally internally reflected, depending on the angle of refraction by the prism, and couple to the fiber. The interaction of light at the prism and fiber facet interfaces can be derived from surface refraction to be:

$$n_1 \sin(\theta_f + \theta_b) = n_2 \sin(\theta_g) \quad (1)$$

$$n_2 \sin(\theta_g' + \theta_f) = n_3 \sin(\theta_f - \theta_t) \quad (2)$$

where in Eq. (1) n_1 is the refractive index of the medium between the ball lens and the prism, n_2 is the refractive index of the prism itself, θ_f is the field angle, θ_g is the angle of refraction with respect to the prism's normal, and θ_b is the blaze angle of the prism. Equation (2) describes the refraction between the prism and the core where n_3 is the refractive index of the fiber core, θ_g' is the angle of refraction after the prism with respect to the optical axis, and the θ_t is the tolerance angle. Note that θ_f is used as both the field angle and the angle of the facet since, as previously stated, the chief ray of each angle is equal to the corresponding facet angle. Solving for the angle of refraction after the prism with respect to the normal for Eq. (2) yields:

$$\theta_g' = \sin^{-1} \frac{n_3 \sin(\theta_f - \theta_t)}{n_2} - \theta_f \quad (3)$$

Using trigonometric identities and substituting the summation of θ_g' and θ_b for θ_g for Eq. (1) yields:

$$n_1 \sin(\theta_f + \theta_b) = n_2 \sin(\theta_g' + \theta_b) \quad (4)$$

$$n_1 \sin(\theta_f) \cos(\theta_b) + n_1 \cos(\theta_f) \sin(\theta_b) = n_2 \sin(\theta_g') \cos(\theta_b) + n_2 \cos(\theta_g') \sin(\theta_b) \quad (5)$$

$$n_1 \sin(\theta_f) + n_2 \sin(\theta_g) = \tan \theta_b (n_2 \cos(\theta_g) - n_1 \cos(\theta_f)) \quad (6)$$

Solving for the blaze angle for a range of field angles yields a variable micro-prism array facet angle as a function of field angle with the following equation:

$$\theta_b = \tan^{-1} \frac{n_1 \sin \theta_f + n_2 \cos \theta_g}{n_2 \cos \theta_g - n_1 \cos \theta_f} \quad (7)$$

The tolerance angle (θ_t) defines the angle of refraction inside the fiber core, and ultimately establishes the angle of divergence when exiting the fiber. For example, if the tolerance angle was set to be 0° the propagation of the chief ray would be on axis with the fiber and reduce the angle of divergence of the chief ray to 0° . This is ideal in terms of output light coupling, but involves performance trade-offs that will be discussed in the next section.

3.2 Moldable radial micro-prism array

It is possible to define a radial microprism array that would be extremely difficult to fabricate, such as one with an unattainable index of refraction. In fact the simplest method of fabrication, and the one most compatible with volume manufacture, is a structure that can be molded or embossed. This creates two facets for the micro-prism array: an input facet, and a release facet. The input facet is the optically functional part of the prism which serves to refract the beam into the fiber core. The release facet is a mechanical constraint of the molding. Complex molding processes or materials may allow for sharply tilted microprisms, or even Fresnel lens like structures that involve total internal reflection [11]. For our design, we assumed that the release facets are arranged perpendicular to the optical axis of the system, allowing for the micro-prism mold master to be pressed into a prism material (e.g., a thermally or UV-curable epoxy) and then removed. However, both the input and release facets are optical surfaces that refract and transmit the focused beam. Rays incident on the input facet refract at angles below the normal of the fiber face to be totally internally reflected and transmitted in the corresponding fiber, while the release facet refract rays larger than the incident angle and result in a loss in coupling efficiency for the corresponding fiber. Unless the microprism pitch is small compared to the optical fiber core diameter, this is a significant factor in prism design. As Fig. 8 illustrates, for a micro-prism array molded in contact with the imaging surface, fibers illuminated only by light passing through the release facet will have low or no signal power. Figure 8(a) depicts a scenario where the scene would vary in brightness periodically, creating an image with fibers that appear to be “on/off”. Alternatively, moving the prism surface further from the image surface and slowly varying blaze angle allows a larger region of the microprism array to be illuminated by a converging beam, dividing the energy between the input and release facets. This distributes power across all fibers because for any field angle two separate focused beams are generated: an enhanced coupling beam from the input facets, and a loss/noise beam from the release facet shown in Fig. 8(b). This loss/noise signal is incident on the fiber bundle at an even larger angle, and so most of the power does not couple to the guided mode. Instead, it propagates in the cladding and through the fibers.

3.3 Micro-prism facet efficiency and micro-prism array design

The divergence of the focused beam when exiting the fiber is dependent on tolerance angle described in Eq. (3). If the tolerance angle is selected to be 0° , the chief ray will refract and propagate directly down the fiber’s axis, minimizing the divergence when exiting the bundle. However, the maximum angle of refraction through the prisms is dependent on the finite index of the microprism material and a 90° maximum fabricable blaze angle. This means that at some point along the field of view the useful facet area of the radial micro-prism array will

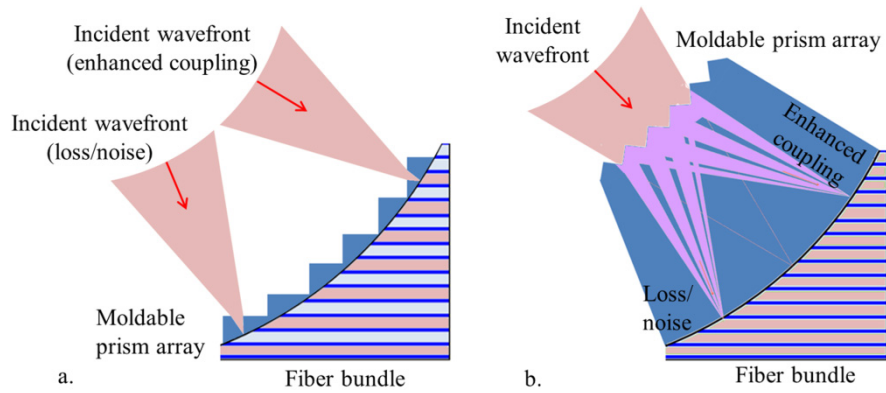


Fig. 8. Illustration of a focused beam incident on a micro-prism array molded on the a) polished input surface of the fiber bundle, b) micro-prism array molded with a non-zero thickness onto the polished fiber bundle. Colored fibers signify coupling from the focusing beam.

no longer be illuminated by any significant portion of the focused beam. On the other hand, the tolerance angle may be selected to be close to the axial critical angle of the fibers, so that the maximum amount of light will propagate inside the fiber. Although the coupling efficiency is maximized, the divergence angle of the rays when exiting the fiber is also at a maximum. The efficiency of the overall system is also determined by the tolerance angle of the prisms and the field of view. The field of view is also considered in calculating the coupling efficiency since projection of the chief ray with respect to the prism facets determines the micro-prism efficiency. The increase in field of view reduces the projection of the input facets due to the increase in blaze angles of prism array. The size of the release facets increase as a consequence of the previous statement, but also due to the increasing field of view along the circular image plane. The efficiency equation is given by:

$$\eta = \frac{P_{in}}{P_{in} + P_{rel}} \quad (8)$$

where η is the efficiency, P_{in} is the projection of the input facet, and P_{rel} is the projection of the release facet, where both projections are towards the center of lens symmetry. The prism should ideally be made of extremely high index of refraction material to minimize the blaze angle required. This reduces the projection of the release facet while simultaneously increasing the projection of the input facet. However, we are limited to commercially available optical epoxies for the micro-prism array. Figure 9 describes the coupling efficiency of the system as a function of field angle and tolerance angle for a fiber core/cladding of 1.81 to 1.48, and a moldable prism with refractive index 1.56. This is the index of refraction of SU-8 photopolymer [12].

If the micro-prism array is selected to guide the chief ray along the fiber optical axis for all angles ($\theta_r = 0^\circ$), the coupling efficiency drops dramatically to zero passed 35° . Since we are attempting to maximize the coupling efficiency, the initialization of the radial micro-prism array does not begin until it reaches the 30° field angle. This means that the facet coupling efficiency is effectively unity until it reaches 30° field of view, as depicted by the black line in Fig. 9(a). As the field of view increases, the tolerance angle remains at 30° throughout the rest of the field of view maximizing the coupling efficiency of the prism for the given micro-prism index material. The blaze angle with respect to the optical axis of the system also increases as the field of view increases, thereby reducing the prism facet efficiency. However, the scene is made brighter with the prisms than without, resulting in an advantage over a polished-bare fiber bundle. The radial micro-prism array's blaze angle will vary as a function of field with a constant pitch of $25\mu\text{m}$ that follows along the radius of the fiber bundle. The choice of

minimum prism pitch reflects the structural accuracy of features formed by low-cost embossing; too short a pitch would mean that the rounding of the prism edges covered a significant fraction of the surface area. The pitch of $25\mu\text{m}$ was chosen as it was the shortest prism pitch available from commercially available micro-prism array sheets, which have been developed for use in liquid crystal display backlighting. For rays to be split across the micro-prism array and prevent dark bands from forming on the transferred image, the cone exiting the ball lens must intercept at least one full period for any field angle. Examining the geometrical spot size in Zemax for a field angle of 52° , we found that a prism substrate thickness of $390\mu\text{m}$ satisfies this constraint.

The final design of the chirped microprism array is shown in Fig. 10 with a constant pitch and using Eq. (3) and Eq. (7) from the previous section to determine the blaze angle as a function of the field of view. The microprism array can be diamond turned in a radial geometry on a master-mold using current manufacturing processes. The surface is smooth up to the field angle of 30° , where the coupled light reaches the limits of the NA 1 fiber transmission. Above the angle, the microprism facets begin. At first, the input facet area is much larger than the release facet area, and the tilt angle is relatively small. As the field angle increases, the fraction of the area needed for prism molding increases, as does the tilt angle needed to keep the signal within the range needed for transmission.

3.4 Optical response of radial micro-prisms

Having used geometrical optics to design the microprism array, our next step is to model the optical response to determine the effect of the segmented aperture on the system impulse response, including diffraction effects. Figure 11 shows the cross section of a FRED simulation employing the optimized micro-prism structure with the glass F/# 4.4 singlet lens (BK7) with a 45° field angle, where we located 3×3 fiber arrays to observe the optical transfer from the two illuminated regions of the curved-face fiber bundle. A single focused signal is split into two beams by facets of the radial micro-prism array. Rays refracted by the input facet are redirected and coupled into the fiber core, whereas rays refracted by the release facet are incident onto a separate 3×3 fiber array and refracted into the cladding. Figure 11(c) shows a polychromatic MTF calculation of the signal beam from the 45° incident light on the surface of the fiber bundle. A drop in resolution can be seen in the tangential plane due to astigmatism from the prism array and chromatic aberrations from the single glass lens and index of the micro-prism (1.56). Using an achromatic lens in conjunction with the micro-prism array can compensate for the chromatic aberrations. The fiber pitch is the limiting factor with a pitch of $8\mu\text{m}$ which corresponds to a maximum resolution of 62.5 cycles/mm. Light refracting into the cladding results in either loss of energy to the system, or noise in additional fibers. Figure 11(d) also shows a significant reduction in divergence of the beam emitted from the fiber, as compared to the beam emitted from an unmodified (spherically polished) fiber bundle for the same field angle. Integrating over the region of the sensor, we quantified an increase in brightness by a factor of 3.2 in comparison to the unmodified fiber bundle. Figure 12 shows that at this field angle, the polished input fiber couples a negligible portion of the focused beam, while the prism facets transfer approximately 50% of the incident energy into the useful coupled mode. The microprism facet apertures that split the focusing beam also cause diffraction, and there is some geometrical aberration caused by the prism itself. The diffraction impulse response shown in Fig. 12 confirms that the microprism sub-aperture, which is effectively rectangular in shape, reduces resolution in the direction perpendicular to the aperture restriction. These effects become more prominent with increasing field.

These calculations show that while microprisms can increase signal intensity at angles greater than 30° relative to a spherically polished fiber bundle, there is also significant loss from the projection of the useful microprism facet at the illuminating field angle. The incident light refracted by the release facet of the microprism is incident on the fiber bundle at even

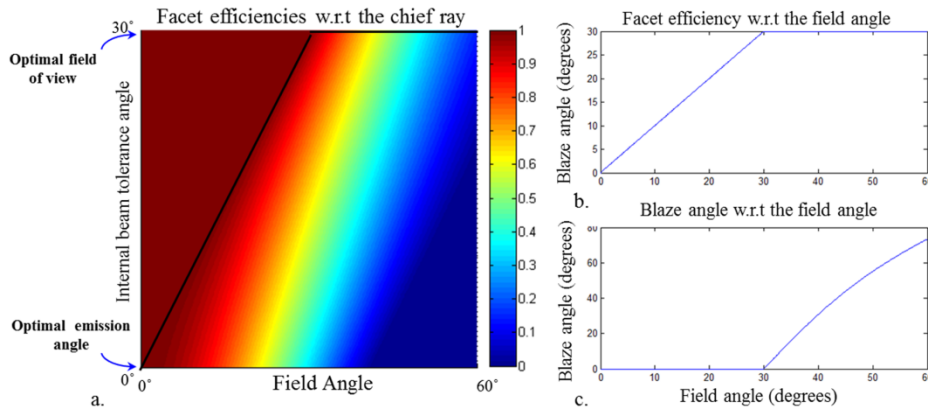


Fig. 9. a) 2-dimensional facet efficiency color plot as a function of field angle and tolerance angle, b) chosen facet efficiency for micro-prism array, c) blaze angle of prism array with respect to the field angle.

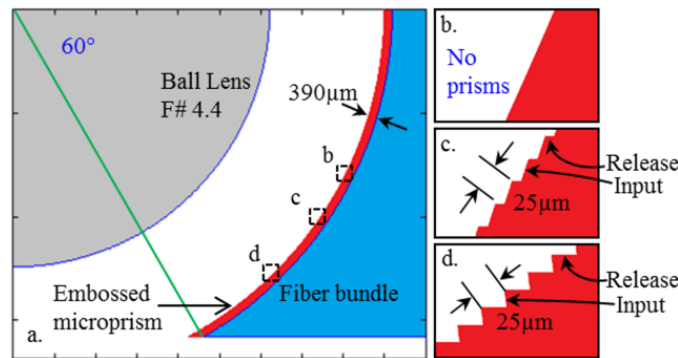


Fig. 10. a) Schematic of ball lens system with an embossed micro-prism array on the input surface of the fiber bundle, b) region with no prisms, c, d) regions with micro-prism array. The microprism array has a thickness of 390 μ m.

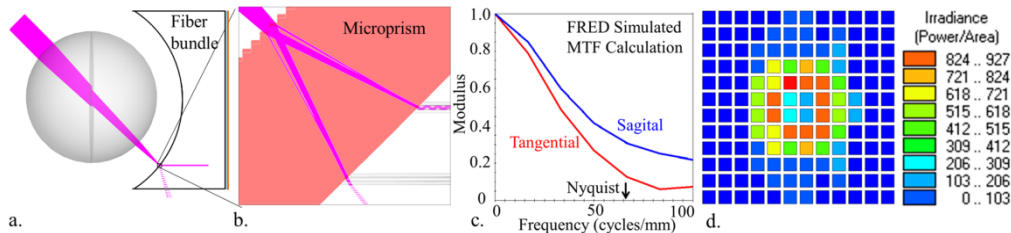


Fig. 11. a,b) Cross section of a 3-D FRED simulation of the micro-prism array increasing coupling efficiency at a field angle (45 $^{\circ}$) larger than the axial critical angle, c) polychromatic MTF calculation of signal beam on surface of fiber bundle, d) irradiance plot on a pixel array.

larger angles, previously shown in Fig. 8(b), and little of this energy can couple to the detector. However, with round fibers some of the energy couples via skew rays, even for very large angles of incidence. So to obtain an estimate of the resulting signal to noise, we quantified the ratio of coupling into the fibers and transmission to the detector between the input and release facets using a ray-based nonsequential FRED simulation. At each field angle, we calculated the energy efficiency through the microprism facet (signal), and also calculated the illumination and coupling (noise) that arrive at this region by refraction of a slightly smaller field angle through the release facet of a nearby region of the microprism

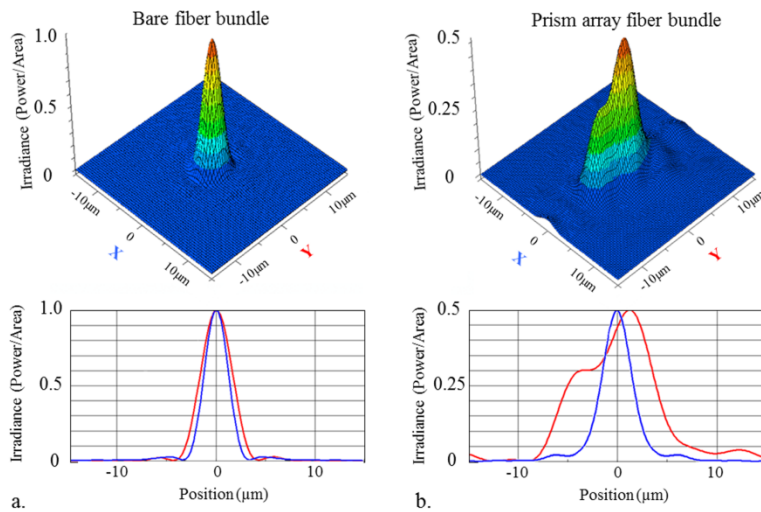


Fig. 12. Irradiance spread function at 45° on surface of the a) polished input fiber bundle, b) input surface of the fiber bundle after being deflected by the prism array.

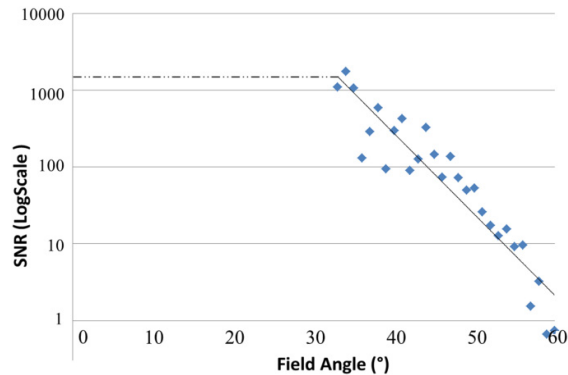


Fig. 13. FRED calculation of signal-to-noise ratio of the input and release facet beams incident on groups of 3×3 fibers.

array, and skew ray coupling through the fiber bundle. The resulting signal to noise ratio at the detector is shown as a function of field angle in Fig. 13. For field angles less than 30° , there is no prism structure, and therefore no source of noise; the high SNR in this region is indicated by a dashed line. Above 30° , the SNR decreases overall as field angle increases. The local SNR depends on where the incident light illuminates the microprism: signal is high when the beam is centered on a useful microprism facet and low where the beam is centered on the release facet. So there is significant local variation in the calculated SNR values. Setting 100:1 (20dB) as a minimum SNR, we see the maximum useful field of view for microprisms embossed with a $25\mu\text{m}$ pitch and this 1.56 index of refraction would be between 90° and 100° . This is a significant increase on the approximately 60° field of view possible using straight fiber bundles. Increasing the microprism index would further increase the useful field of view.

4. Proof of concept system

To demonstrate microprism-enhancement of fiber coupling, we made a monocentric singlet lens and illuminated a straight N.A. 1 fiber bundle where the concave input surface covered over 100° field of view, nearly double the angular acceptance possible with a smooth

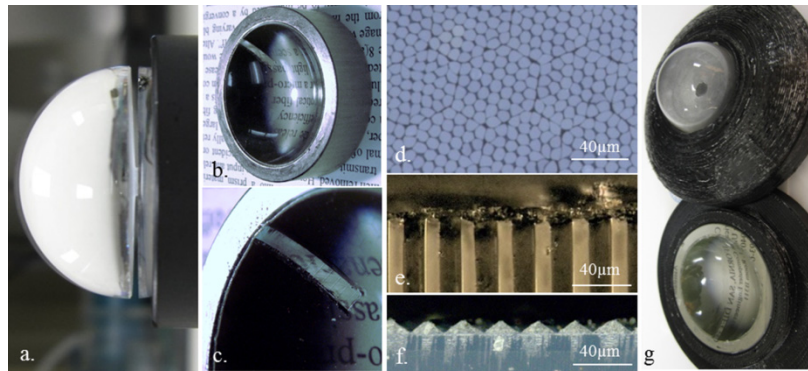


Fig. 14. a) F/# 4.3 BK7 ball lens, b) curved-face fiber bundle with microprism array, c) close up of microprism array, d) microscope image of fiber, e) top view of molded micro-prism array structure, f) cross-section of Vikuiti BEF II 90/24 microprism array, g) ball lens and fiber bundle in 3D printed mount.

spherical surface. The optimized design shown in Fig. 10 calls for a chirped spatial period prism structure, and the best way to test signal coupling is with a high resolution focal plane index matched to the rear surface. For this first proof of principle, we fabricated microprism structures by embossing local regions of SU-8 photoresist with a constant spatial period linear prism array mold, and recorded the transmitted image by relay imaging the back surface of the fiber bundle onto digital SLR camera.

We constructed an F/4.3 monocentric singlet lens by cutting an aperture stop into a solid 24.24mm diameter BK7 sphere. The aperture was formed by cutting a deep slot into the perimeter of the lens with a diamond saw, rotating the lens until only a post approximately 2.80mm diameter remained at the center, then filling the kerf with black shims and UV-cured optical adhesive to block stray light and retain structural integrity. The result was a lens with a focal length of 17.8mm, and with a ZEMAX modeled $9.76\mu\text{m}$ RMS spot radius and 48 lp/mm at MTF50 for polychromatic light. The lens was tested using a NA 1 fiber bundle polished with a spherical input surface of radius 17.8mm and a flat output surface. The fibers were arranged in an irregular hexagon closely-packed array with a 7 to 8 μm pitch, indicating a Nyquist-limited resolution of approximately 70 lp/mm. The singlet lens and fiber bundle were attached to two sides of a 3D printed mount, threaded to allow for focus, seen in Fig. 14.

We obtained a periodic linear prism array with a constant blaze angle of 45° and a pitch of $25\mu\text{m}$ from 3M (Vikuiti BEF II 90/24). Ideally, the microprism array should be made of annular rings and a variable blaze angle, but this structure is approximately correct for a small region of our design at a 45° field angle. A 2mm thick strip of the prism was molded onto a spherical polydimethylsiloxane (PDMS) handle with an approximate radius of 17.80mm. This negative PDMS mold was then used to make the positive spherical mold of optical adhesive ($n = 1.56$) onto the fiber bundle with the desired thickness of 0.390mm by offsetting the PDMS mold from the polished input surface of the fiber bundle. The molded prism was positioned on wide field of view regions from approximately 27° to 52° . PDMS was used as the molding material in order to prevent adhesion of the mold to the adhesive during lift off. The central aperture of the fiber bundle (the surface covering a field of view less than 27°) did not have a prism array, and instead had a spherical corrective surface to equalize the optical path length for all fields. Figure 14(f) shows the embossed microprism facets.

The imager was arranged 2 meters away from a wall covered with an assortment of resolution targets. In a similar setup to that used when measuring the divergence of the fiber bundles, we used a Canon DSLR camera with an F/2.8 lens to capture the image formed by the monocentric fiber coupled system. One limitation of this arrangement is that the light emitted from the fiber bundle can cover an angular extent far larger than the 10° half field of view captured by the F/2.8 relay lens. The final fiber-coupled imager for this focal length will

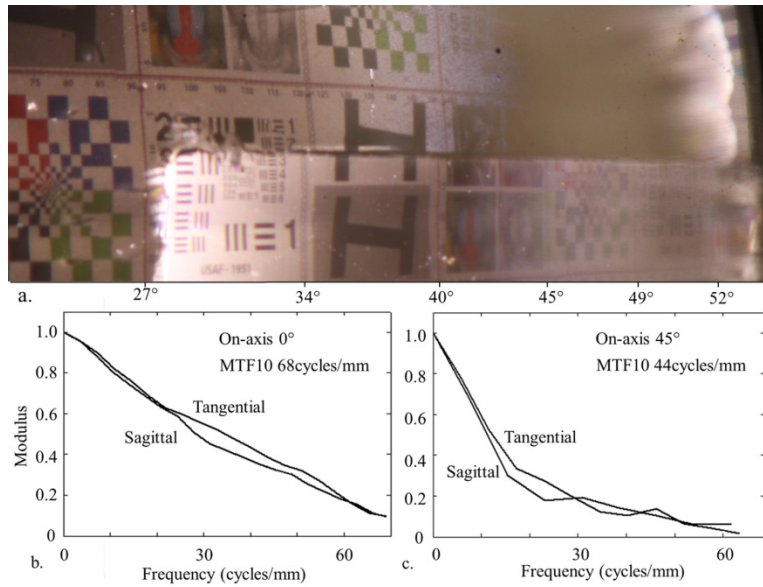


Fig. 15. a) Photograph of image transferred through fiber bundle both with a smooth spherical surface (upper half) and with a molded prism (lower half) over the region from 27° to 52° field angle. The prism array extends the field of view where the polished bundle no longer transmits a significant signal. b,c) Slant edge chart MTF measurements at on-axis and 45° off axis.

use a large format (full frame) CMOS image sensor, but the cost of this type of sensor did not allow their use for these proof-of-principal tests of microprism structure. Measuring the on-axis performance using Imatest software for the polished-bare fiber bundle produced a baseline resolution of 68cycles/mm at a modulus of 0.1 for our system, confirming that the fiber bundle rather than the lens was the resolution limit.

Figure 15(a) shows the spherically corrected surface directly above the sectioned microprism array to have noisy background in the wider field of view areas. Since the fibers are closely packed and dense, rays that do not couple into the fibers are refracted and reflected in other core/cladding regions, effectively becoming stray light and background noise for other fields. These are the same areas where the coupling efficiency for the bare fiber bundle has dropped significantly, and background noise dominates most the image scene. Figure 15(b) shows a comparison of the resolution for the molded prism bundle revealing no significant changes on axis for the spherical corrective region. Shifting the camera to the region of the prism array captures light form both the spherically corrected and prism molded surface for comparison in resolution seen in Fig. 15(c). A resolution of approximately 44 cycles/mm at a modulus of 0.1 was measured at the 45° field of view region for the calculated signal enhancement blaze angle. Aberrations associated with the prism array, in addition to any imperfections in the molding process, caused a decrease in resolution in contrast with the on-axis MTF. Overall, however, it is clear that the region of microprism array has increased the field of view while maintaining some resolution, and considerably decreased the noise that would have otherwise been present from the uncoupled rays.

The output of the fiber bundle has a transition from high-index fiber core to air, which prevents some large-angle rays coupled into the fiber from exiting. To provide a more representative sample of the transferred image we molded an 80° holographic diffuser using PDMS on the output surface of the fiber bundle. This causes the light incident on the rear surface of the fibers to scatter into a wide angle, reducing signal power at any given field position, but allowing a single image to capture the full field. The diffusive surface was on the order of tens of microns, reducing the resolution of our image, but provided an observation of

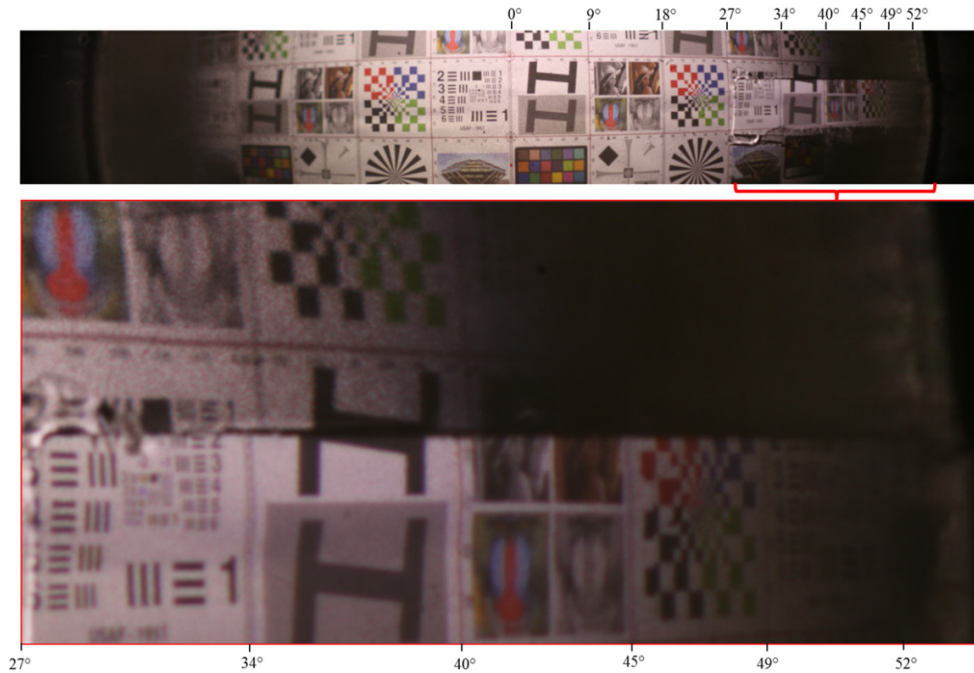


Fig. 16. Stitched image of prism array molded bundle with a diffusive output surface. The image was stitched from several images at a constant 1 sec exposure and ISO 400.

enhanced signal coupling from the prism array. Figure 16 shows a panoramic image of stitched images taken by shifting the relay camera across the fiber bundle. Close examination of the prism array regions reveals the brightness significantly enhanced, and noise reduced, in the wide field of view in comparison to the spherically corrected region above. We measured the intensity at the 45° field of view of a white background image to be brighter by approximately a factor of 3 in comparison to the polished region, confirming our results in simulation from the previous section.

5. Conclusion

We have shown that the field of view possible for images coupled from a spherical field of view via straight fiber bundles can be significantly enhanced using a beam-deflecting structure close to the spherical image surface. Monocentric fiber coupled imagers benefit from a radially symmetric system that do not suffer from coma or astigmatism, and can be utilize a curved image plane. This beam-deflection can be accomplished by multiple types of structures, both refractive and diffractive. We described analysis and an experimental proof-of-principle investigation of the use of microprisms directly embossed onto the spherical fiber bundle. The optimum embodiment of this general concept may involve diffractive, rather than refractive beam deflections. One method is to create a chirped volume hologram located near to the image surface. Another direction is the use of surface plasmon antennas directly on the image surface, in contact with the high index fibers [13]. These techniques offer for the volume manufacture of fiber-coupled wide-field imagers, which may ultimately support the wafer-scale fabrication of fiber-coupled image sensors for low-cost wide-angle imaging.

Acknowledgments

This research was enabled by support from the DARPA SCENICC program, contract W911NF-11-C-0210, and from Motorola ATAP and Google's Advanced Technology and Projects group. I'd also like to acknowledge members of PSI Lab for their support and contributions.